Biosensors and Bioelectronics 146 (2019) 111738

Contents lists available at ScienceDirect

Biosensors and Bioelectronics

journal homepage: http://www.elsevier.com/locate/bios

Enhanced surface plasmon microscopy based on multi-channel spatial light switching for label-free neuronal imaging

Taehwang Son [a], Changhun Lee [a], Gwiyeong Moon [a], Dongsu Lee [b], Eunji Cheong [b], Donghyun Kim [a,*]

[a] School of Electrical and Electronic Engineering, Yonsei University, Seoul, 03722, South Korea
[b] Department of Biotechnology, Yonsei University, Seoul, 03722, South Korea

ARTICLE INFO

Keywords:
Surface plasmon
Surface plasmon microscopy
Label-free imaging
Light-switching
Neuron

ABSTRACT

In this paper, we have investigated multi-channel switching of light incidence in multiple directions to improve image clarity in surface plasmon microscopy (SPM) for robust and consistent imaging performance regardless of the pattern geometry and shape. Multi-channel light switching in SPM allows significant reduction of adverse scattering effects by surface plasmon (SP). For proof of concept, an eight-channel spatially switched SPM (*ss*SPM) system has been set up. The results with reference objects including square arrays and Siemens stars experimentally confirm much improved images with *ss*SPM by reducing the artifacts of SP scattering significantly. On a quantitative basis, contrast analysis preformed with square arrays shows image contrast enhanced by more than three times over conventional SPM. Three image reconstruction algorithms were evaluated for optimal image acquisition. It is suggested that averaging combined with minimum-filtering produces the highest resolution. *ss*SPM was applied to label-free imaging of primary neuron cultures and shown to present enhanced images with clarity far better than conventional SPM.

1. Introduction

Human desire to observe small objects that are invisible to naked eyes has been the driving force behind the development of optical microscopy. One of such techniques is surface plasmon microscopy (SPM) (Hickel et al., 1989; Rothenhäusler and Knoll, 1988), which visualizes the intensity changes as a result of refractive index variation in the evanescent field when surface plasmon (SP) is excited at metal dielectric interface by being momentum-matched with incident photon. Unlike bright-field microscopy, SPM may selectively visualize an event within penetration depth of the evanescent wave similar to TIRF microscopy. Because SPM does not rely on labels as a dark-field imaging method which operates near or under SP resonance (SPR), it has been used in many biomedical engineering studies, for example, to investigate cell adhesion (Giebel et al., 1999; Peterson et al., 2014; Soon et al., 2013; Watanabe et al., 2012a), cell substrate interactions (Moh et al., 2008; Peterson et al., 2009; Su et al., 2010; Wang et al., 2012a), intracellular molecular dynamics (Shinohara et al., 2013; Wang et al., 2012b; Yang et al., 2015.), cellular structures (Berguiga et al., 2011; Yanase et al., 2010), lipid vesicle adsorption (Jenkins et al., 2001), and cell-electrode gap (Toma et al., 2014). SPM also found uses in chemical and material science for visualization of binding reactions (Piscevic et al., 1995) and electrochemical potential waves and currents (Flätgen et al., 1995; Shan et al., 2010), characterization of crystalline domains (Kooyman and Krull, 1991) and thin films (Knobloch et al., 1996), and quantification of refractive index changes (Kotsev et al., 2003) and local distances (Zhang et al., 2001). In addition, efforts have been made to merge SPM with other detection methods such as surface-enhanced Raman scattering (Meyer et al., 2012), spectroscopy (Yuk et al., 2008), and atomic force microscopy (De Hollander et al., 1995).

One critical problem of SPM is poor image resolution due to SP scattering of light. SP propagation length (L_{sp}) often ranges from 10 ~ 100 μm (Lamprecht et al., 2001), which causes the resolution of SPM to be much worse than the diffraction limit. Various approaches have been taken to improve the resolution in SPM (Laplatine et al., 2014; Thariani and Yager, 2008; Vander and Lipson, 2009), for example, based on the optimization of optical components (Berger et al., 1994; De Bruijn et al., 1993; Jamil et al., 2008; Somekh et al., 2000) and nanoplasmonic control of SP propagation (Kim and Kim, 2010; Smolyaninov et al., 2006). Scanning-based SPM was shown to produce near

* Corresponding author.
E-mail address: kimd@yonsei.ac.kr (D. Kim).

https://doi.org/10.1016/j.bios.2019.111738
Received 28 August 2019; Accepted 27 September 2019
Available online 30 September 2019

diffraction-limited resolution using x/y raster scanning with a sample stage at the expense of much slow imaging acquisition (Watanabe et al., 2012b).

Recently, simple two-channel spatially switched SPM (*ss*SPM) was proposed to achieve much improved image resolution in SPM (Son et al., 2018a), in which images are acquired with incident light illuminated in opposite directions while maintaining the angle of incidence and polarization and minimum-filtered for post-processing. More details of the operation principle are described in Supporting Information S1 for the simplest model. The two-channel ssSPM was extended to momentum-sampling based on galvanometer scanning (Kuai et al., 2019). Multichannel SPM was partially demonstrated without modification of optical set-up using sample rotation and image registration (Banville et al., 2018). However, this method suffers from inherent image misregistration, which may limit the application to imaging sub-micron features. Plasmonic light switching was also shown to be useful for super-resolved fluorescence microscopy (Kim et al., 2010; Son et al., 2018b). In fact, spatial switching in *ss*SPM can be understood as momentum sampling of the spatial domain. In this sense, improvement of resolution by spatial light switching in SPM can find analogy in other imaging techniques, most notably, structured illumination microscopy, which enhances spatial resolution by sampling Fourier domain outside the observable frequency space (Gustafsson, 2000). Similarly, synthetic aperture microscopy has been investigated to enhance spatial resolution without labels by broadening the range of spatial frequency achievable in the Fourier domain (Choi et al., 2007; Cotte et al., 2013; Schwarz et al., 2003). By analogy, Fourier ptychography was adopted to enhance spatial resolution using a low NA objective lens and an incoherent light source with a good field of view (Guo et al., 2015; Zheng et al., 2013), although its performance is limited compared to commercial microscopes with an oil-immersion high NA objective (Ou et al., 2015).

Despite the possibilities, *ss*SPM may only be effective for single-axis linear objects because of the nature of two-channel switching, i.e., the minimum-filtering works with the lowest noise when a scattering edge is orthogonal to the direction of plasmon scattering. Also, the two-channel *ss*SPM needs the distance between patterns to be longer than SP propagation length to avoid crosstalk. For this reason, we intend here to improve conventional SPM images of objects with complex multi-directional structures and to generalize *ss*SPM for clear visualization of arbitrary morphology. An obvious approach to attain this goal is to increase the number of channels for enhanced control of spatial frequency components. An important question is how many sampling channels are sufficient for imaging an object of any shape. *ss*SPM with a larger number of channels represents sampling in a larger area in the Fourier space. The effectiveness of *ss*SPM depends on the size of frequency content of an object. Assuming that an object is not bandlimited, although the marginal utility accompanied by the increase of the channel number would decrease, an increased number of switching

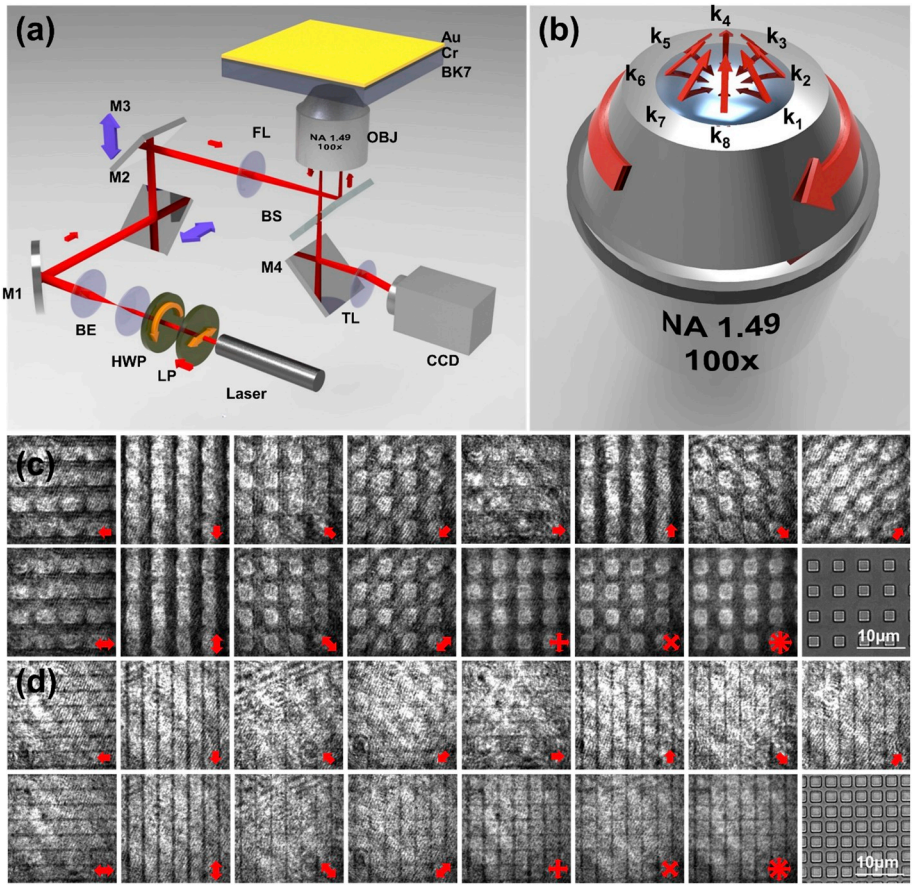

Fig. 1. (a) Optical set-up of multichannel *ss*SPM (LP: linear polarizer, HWP: half wave plate, BE: beam expander, M1, M2, M3, and M4: mirrors, FL focusing lens with $f = 200$ mm, OBJ: objective lens and TL: tube lens). Arrows for M2 and M3 represent displacement of the mirrors. (b) Conceptual illustration of switched light illumination in eight-channel *ss*SPM ($n = 8$). k_i with $i = 1 \sim 8$ represents the wave vector corresponding to each of the eight directions of switched light incidence. The arrow around the objective lens denotes clockwise temporal sequence of light switching. Images of reference square arrays by conventional SPM (⬅,⬇,⬉,⬈,➡,⬆,⬊,⬋), two-channel (⬌,⬍,⬊,⬈), four-channel (+,×), and eight-channel *ss*SPM (✳): (c) array period $\wedge = 5$ μm and square width $w = 2$ μm and (d) $\wedge = 3$ μm and $w = 2$ μm.

channels would always lead to the improvement in the image quality, which is ultimately limited by the diffraction-limit, and can reduce various artifacts due to crosstalk and pattern orientation that under-sampled SPM may exhibit and improve the utility at the expense of growing complexity (see Supporting Information S2). Our analysis shows that a design based on eight channels provides sufficient compromise between complexity and performance. The results were confirmed by imaging reference objects and neurons.

2. Results and discussion

2.1. Multi-channel ssSPM images of square arrays

The optical schematic for the *ss*SPM set-up is presented in Fig. 1(a). Details of the set-up can be found in Supporting Information S3. The eight-channel *ss*SPM ($n = 8$) samples the spatial frequency of an object field in eight channels by illuminating with different $\boldsymbol{k}$ vectors as shown in Fig. 1(b). SP scattering is dominant along the direction in parallel to SP propagation and tends to be insignificant in the perpendicular direction (see Supporting Information S4 and S5). Multi-channel *ss*SPM ($n > 2$) can exploit the minimal SP scattering in the perpendicular direction under different illumination switching conditions and enable to resolve objects in the direction of SP propagation. This method can address the limited applicability of two-channel *ss*SPM. Fig. 1(c) and (d) show SPM images of reference square arrays for an array period $\wedge = 5$ and 3 μm when the square width is fixed at $w = 2$ μm (fabrication described in Supporting Information S6). Clearly, the images acquired by eight-channel *ss*SPM present much better resolved squares than those from conventional SPM and two-channel *ss*SPM. The improvement is, in fact, more significant with the distance between objects. Note that the geometric parameters such as period, width, and gap between squares ($\wedge - w$) are smaller than SP propagation length: nonetheless, image acquisition works by multi-channel spatial switching combined with reconstruction processes. Image analysis suggests significantly enhanced contrast by 3.05 (= 37.5/12.3 in 8-bit intensity, sample number: 218) and 1.61 (= 37.5/23.3, sample number: 218) times over conventional SPM and two-channel *ss*SPM (see Supporting Information S7 for more details of contrast analysis). Note that relative standard deviation (RSD) decreases from 2.52 to 1.17 and 0.395, as the channel number increases from $n = 1$ to 2 and 8, which implies improved image quality with a larger number of channels with *ss*SPM. Such enhancement by eight-channel *ss*SPM was found to be repetitive and robust on the order, regardless of the specific way that it was measured. Substantial enhancement in the contrast can be translated into an improved signal-to-noise ratio as a result of reduced SP scattering. Fig. 1(c) and (d) clearly demonstrate that multi-channel *ss*SPM allows imaging samples consisting of internal structure with a size which would have been extremely difficult with conventional SPM (even with two-channel *ss*SPM).

2.2. Experimental confirmation of multi-channel ssSPM with reference objects

Fig. 2(a) shows a bright-field microscopy image of a Siemens star (30-μm size) with 12 spokes, which we used as a reference object to assess the effectiveness of multi-channel *ss*SPM. Fig. 2(b) and (c) show images of the Siemens star in single-channel conventional SPM, while the two-channel *ss*SPM image is presented in Fig. 2(d). The region marked by the blue arrow in Fig. 2(b) is resolved, while the one marked by the green arrow in Fig. 2(c) is distinguished. While these regions can be resolved by switching in two-channel *ss*SPM, the region marked by the yellow arrow remains blurred as shown in Fig. 2(d). The two-channel *ss*SPM image, as well as those acquired by conventional SPM, is clearly insufficient to remove the image blurring artifacts due to SP scattering. This is because an optimal imaging condition is not fulfilled when the target arrangement and the direction of the incident wave

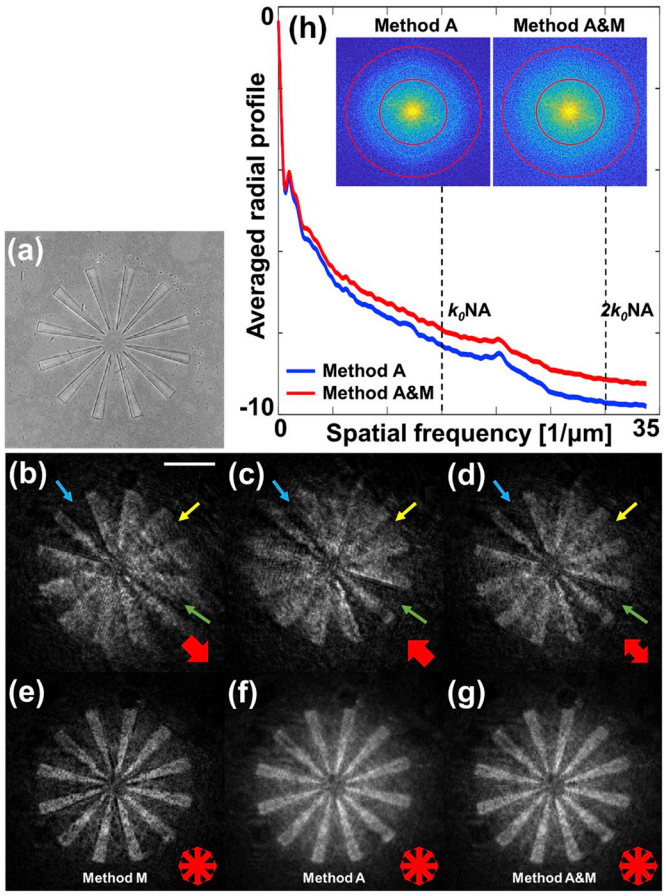

Fig. 2. (a) Bright-field image of a Siemens star (30-μm size) with 12 spokes. (b, c) SPM images of a Siemens star with different directions of light incidence. Scale bar: 10 μm. (d) Two-channel *ss*SPM images reconstructed from (b) and (c). The region marked by the blue arrow is resolved in (b), while the one marked by the green arrow is distinguished in (c). The region marked by the yellow arrow remains unresolved in neither of (b) and (c) in two-channel *ss*SPM. (e–g) Eight-channel *ss*SPM images with different reconstruction methods: (e) eight channel minimum filtering, (f) eight channel averaging, and (g) minimum filtered two channel averaging. Red arrows of (b–g) mark the direction of light incidence. (h) Averaged radial profiles along the azimuthal direction of the Fourier transform. The magnitude on the y-axis is on a logarithmic scale. Inset: Fourier transform of SPM images of a Siemens star in eight-channel *ss*SPM images with averaging (Method A) and minimum filtered two channel averaging (Method A&M). Concentric red circles in the inset represent the spatial frequency of k_0NA and $2k_0$NA in the Fourier domain. (For interpretation of the references to colour in this figure legend, the reader is referred to the Web version of this article.)

vector ($\boldsymbol{k}_i$) are not perpendicular. Improvement of resolution was attained by extending minimum filtering for multi-channel SPM images so that the highest achievable spatial frequency information can be selectively exploited depending on the channel.

For this purpose, we have used eight-channel *ss*SPM based on three image reconstruction methods: minimum filtering (Method M shown in Fig. 2(e)), simple averaging (Method A in Fig. 2(f)), and minimum filtered two channel averaging (Method A&M in Fig. 2(g)), in which averaging is performed after minimum-filtering opposite channels. More details of the three image reconstruction methods can be found in Supporting Information S8. Eight-channel minimum filtering provides the sharpest edges by best conserving the high spatial frequency information as presented in Fig. 2(e). While the advantages of minimum filtering were confirmed in two-channel *ss*SPM (Son et al., 2018c), the algorithm using multi-channel images ($n > 2$) is likely to lose signal intensity at some pixels in the presence of coherent speckle noise by

scattering dust particles or surface imperfections. On the other hand, averaging is the simplest reconstruction method, in which all eight-channel images are averaged. Despite the simplicity, strong background blur due to SP scattering remains substantial in the area between spokes of the Siemens star, as shown in Fig. 2(f). Therefore, we have implemented a hybrid method of minimum-filtering two-channel images and then averaging four minimum-filtered images to synthesize the Fourier domain, as shown in Fig. 2(g).

The reconstruction process can be better understood in the Fourier domain, as we have presented in Fig. 2(h). Inset shows Fourier transform images of the Siemens star in eight-channel *ss*SPM based on the image reconstruction by Method A and A&M. The reconstruction by Method M tends to be dominated by the channel with significant intensity loss as described in Methods, thus was excluded from Fig. 2(h). Low frequency components represent blur while strong high frequency improves image clarity, although it also emphasizes artifacts such as speckle. Simple averaging (Method A) shows mild high frequency components with strong presence of low frequency blur. On the other hand, the Fourier spectrum obtained by minimum-filtering suggests a broad Fourier spectrum with relatively weak low frequency components. The complementarity between Method A and M leads to the combination into a Fourier spectrum shown in Fig. 2(h) for Method A&M.

For the quantitative evaluation, we define an averaged radial profile (ARP) as the amplitude sum of an image in the Fourier space over the ring-shaped radial profile shown in Fig. 2(h) in the range of $k_0\mathrm{NA} < f_r < 2k_0\mathrm{NA}$ (f_r: radial spatial frequency in the polar coordinate representation), i.e.,

$$\mathrm{ARP} = \int_{k_0\mathrm{NA}}^{2k_0\mathrm{NA}} \int_0^{2\pi} L(f_r, f_\theta)\, df_\theta df_r \tag{1}$$

$$L(f_r, f_\theta) = |F\{object\} A(f_r, f_\theta)| \tag{2}$$

where $F\{\}$ denotes Fourier transform operation of an object and $A(f_r, f_\theta)$ is the amplitude transfer function of the optical system. The integration range in Eq. (1), where $k_0\mathrm{NA}$ corresponds to the diffraction-limited cutoff frequency, was selected to exclude low frequency blur and high frequency artifacts. Overall, $L(f_r, f_\theta)$ is the Fourier transform amplitude at a specific spatial frequency evaluated in the image plane. ARP is an indirect measure of image quality representing high frequency information without blur which affects the final image. In this sense, higher ARP may lead to enhanced spatial resolution. In Fig. 2(h), ARP(Method A&M)/ARP(Method A) = 1.51, which suggests improved SPM image reconstruction with Method A&M over Method A by more than 50%.

2.3. Neuronal imaging with multi-channel ssSPM

The multi-channel *ss*SPM has been applied to the visualization of dried cortical neuron. Preparation of neuron is detailed in Supporting Information S6. Fig. 3 presents conventional SPM and eight-channel

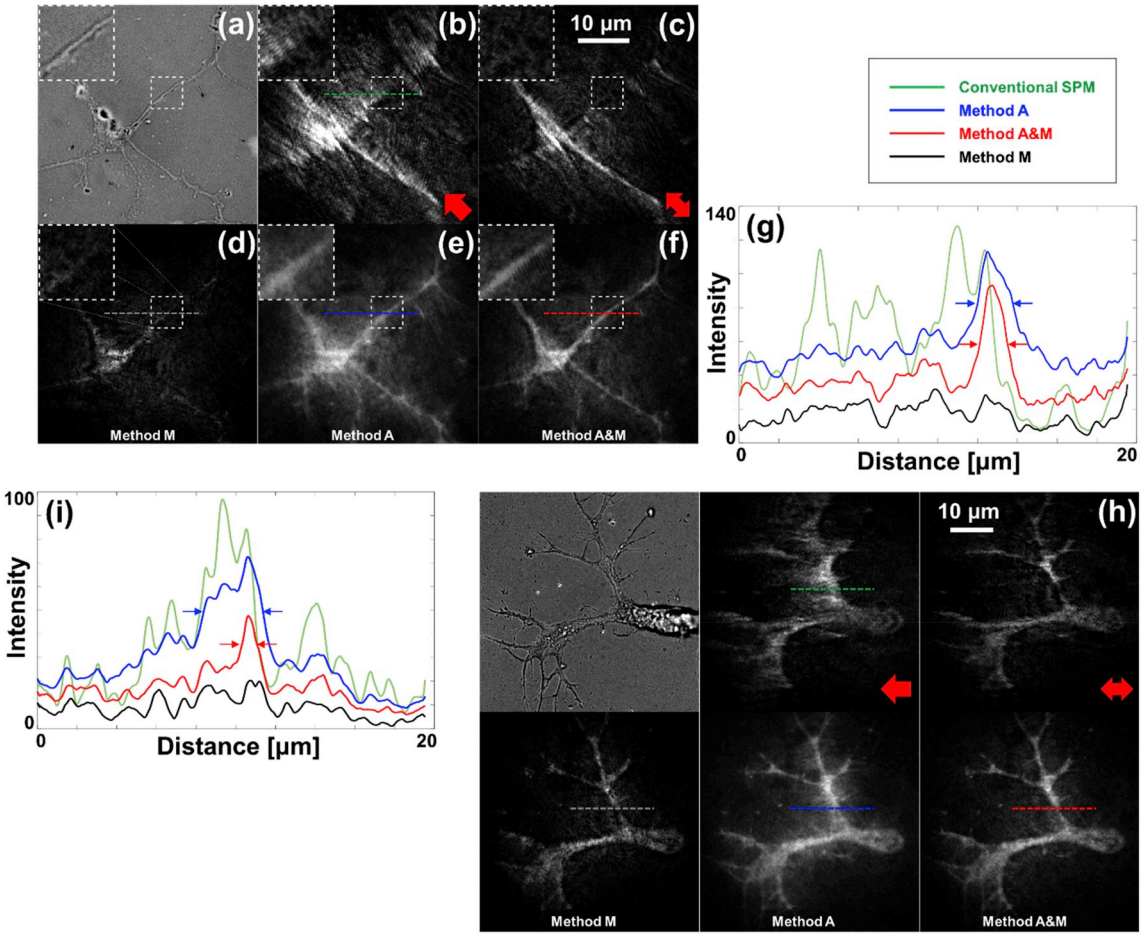

Fig. 3. Images of a cortical neuron by eight-channel *ss*SPM: (a) Bright-field image of the neuron. (b) Conventional SPM and (c) two-channel *ss*SPM image of neuron. Red arrow marks the direction of light incidence. (d) Eight channel minimum filtering (Method M), (e) eight channel averaging (Method A), and (f) minimum filtered two channel averaging (Method A&M). Dotted square represents a magnified image of neuronal axon in an identical location. (g) Intensity distribution across neuronal axon (dotted line in b, d-f) with respect to the image reconstruction methods compared to conventional SPM. (h) Bright-field, SPM, and *ss*SPM images of another neuron. (i) Intensity distribution across neuronal axon (dotted line in h). (For interpretation of the references to colour in this figure legend, the reader is referred to the Web version of this article.)

*ss*SPM images of a neuron with a bright-field microscope image in Fig. 3 (a). As shown in Fig. 3(b), neurites placed along the direction parallel to light illumination were found to be brighter than along the perpendicular direction. However, blurring also became significant along the parallel direction and, therefore, makes it almost impossible to recognize the spatial information along the direction of light illumination. In contrast, neurites placed along the perpendicular direction can be better identified. Even after minimum filtering in two-channel *ss*SPM shown in Fig. 3(c), it was difficult to obtain morphological variation along the SP propagation directions. This is mainly because of higher complexity of an object than the Siemens star. On the other hand, we emphasize that with an increasing the number of channels, a whole morphology of neuron can be quite clearly observable as shown in Fig. 3(d–f), i.e., multi-channel *ss*SPM enables visualization of complex details of neuron which would be impossible with conventional SPM.

Considering that SPM images represent cell adhesion (Giebel et al., 1999; Son et al., 2018c), the neuron presented in Fig. 3 appears to be well attached to the surface, although the clarity differs depending on the image reconstruction methods. In general, the difference between the three image reconstruction methods is much starker for neurites than for the Siemens star of Fig. 2 because of the complexity of a cell. Although eight-channel averaging (Method A) in Fig. 3(d) presents a reasonably good reconstructed image along all the azimuthal directions with relatively blurred edges. On the other hand, minimum filtering (Method M) presented in Fig. 3(e) emphasizes the critical problem of losing details of cell morphology, which is caused by intensity loss while finding the minimum value of each pixel. It is thus suggested that an eight-channel minimum filter may not be applied for general purposes. On the other hand, the hybrid image reconstruction method based on minimum-filtering and averaging (Method A&M) shown in Fig. 3(f) presents much enhanced result in agreement with the case of the Siemens star. The method produces an image with better image contrast than eight-channel averaging. The image is also error-free compared to the one reconstructed by minimum filtering.

For quantitative evaluation, intensity distribution across neuronal axon corresponding to the dotted lines in Fig. 3(d–f) is shown in Fig. 3(g) obtained with different image reconstruction methods. In conventional SPM and *ss*SPM with image reconstructed by minimum-filtering (Method M), we were unable to find a distinct peak that corresponds to the axon. In contrast, an intensity peak corresponding to axon was clearly identified by *ss*SPM after reconstruction by averaging (Method A) or minimum-filtering and averaging (Method A&M). These trends were largely similar in other parts of the neuron and another neuron as shown in Fig. 3(h) and (i). If we define contrast (C) as the peak-to-background intensity difference (details of the statistical analysis described in Supporting Information S9), $C = 82.1 \pm 17.5$ (Method A) vs. 81.3 ± 8.5 (Method A&M) and the background noise intensity itself was measured to be 75.1 ± 9.7 vs. 35.1 ± 3.0 (in 8-bit intensity). In other words, while background noise is significantly reduced by 53.3% (= (75.1–35.1)/75.1) after image reconstruction with Method A&M, peak intensity is also reduced by an amount commensurate with this reduction so that the obtained contrast was almost identical between Method A and A&M. Full-width-at-half-maximum (FWHM) decreased to 1.97 ± 0.73 μm with Method A&M, compared to 2.70 ± 0.49 μm with Method A, a decrease by 27% (= (2.70–1.97)/2.70). The results confirm that the hybrid reconstruction (Method A&M) performs the best and achieves both good contrast and FWHM. Despite considerable improvement in contrast by Method A and A&M, it is much lower than the improvement that we observed with reference square arrays in the previous section. This is caused by the difference in the shape of neuronal axon from the square array, i.e., the edge that defines the axon is smooth while squares have relatively abrupt edges.

Overall, the use of eight-channel *ss*SPM allows anatomical characteristics of a neuron, such as the projection of axons and dendrites, to be clearly identified, which would in general be extremely difficult with conventional SPM. The eight-channel ssSPM can be easily extended to imaging cells under normal buffer ambiance with improved stage control, in which case higher resolution may be obtained because of reduced L_{sp}. Spectral analysis was performed for additional account of improvement by eight-channel *ss*SPM based on Fourier transform images of neuron as well as the radial intensity averaged over $k_0\mathrm{NA} < f_r < 2k_0\mathrm{NA}$, as provided in Supporting Information S10.

2.4. Discussion

The resolution in *ss*SPM is not limited by SP scattering, therefore much enhanced over conventional SPM. Background noise and deleterious interference unrelated to SP scattering remain to affect the resolution even after image reconstruction by minimum-filtering, i.e., the effect of channel number on the resolution is weak in *ss*SPM. Nonetheless, the advantages of multi-channel *ss*SPM are clear in the sense that imaging of an object with arbitrary shape including circles and complex geometry and internal structure that is much smaller than SP scattering length is readily available. Multi-channel *ss*SPM provides much improved image clarity to distinguish an object in the presence of impurities that may affect the quality of an image. Most importantly, we emphasize that the significance of this study can be understood as a milestone to reach high resolution 3D SPM imaging. Without point scanning, an image with a wide field-of-view may by acquired simultaneously with multi-channel switching and/or angle scanning.

3. Conclusions

We have investigated multi-channel *ss*SPM to remove artifacts of severe SP scattering, which restricts the use of conventional SPM. Multi-channel *ss*SPM takes advantage of switching light incidence in multiple directions for robust and consistent imaging performance regardless of the pattern geometry and shape. An eight-channel *ss*SPM system was set up for visual assessment with reference objects such as square arrays and Siemens stars and applied to imaging neurons. Contrast analysis confirmed significant enhancement by more than three times using eight-channel *ss*SPM over conventional SPM with much reduced scattering artifacts. Three image reconstruction algorithms were evaluated for optimal image acquisition, i.e., minimum-filtering (Method M), averaging (Method A), and averaging and minimum-filtering (Method A&M), among which Method A&M was shown to outperform the other image reconstruction algorithms. Further improvement should be made to achieve higher image resolution by optimized noise management.

Author statements

TS designed and performed experiments and wrote the draft. GM calculated SP scattering models. CL fabricated reference samples. DL and EC cultured neuron and performed cell imaging experiments. DK analyzed the data and wrote the manuscript. Authors declare no conflict of interest, nor any competing financial interests.

Declaration of competing interest

The authors declare that they have no known competing financial interests or personal relationships that could have appeared to influence the work reported in this paper.

Acknowledgment

This work was supported by the National Research Foundation grants funded by the Korean Government (2019K2A9A2A08000198 and 2019R1F1A1063602).

Appendix A. Supplementary data

Supplementary data to this article can be found online at https://doi.

org/10.1016/j.bios.2019.111738.

References

Banville, F.A., Moreau, J., Sarkar, M., Besbes, M., Canva, M., Charette, P.G., 2018. Opt. Express 26, 10616–10630.
Berger, C.E., Kooyman, R.P., Greve, J., 1994. Rev. Sci. Instrum. 65, 2829–2836.
Berguiga, L., Roland, T., Monier, K., Elezgaray, J., Argoul, F., 2011. Opt. Express 19, 6571–6586.
Choi, W., Fang-Yen, C., Badizadegan, K., Oh, S., Lue, N., Dasari, R.R., Feld, M.S., 2007. Nat. Methods 4, 717–719.
Cotte, Y., Toy, F., Jourdain, P., Pavillon, N., Boss, D., Magistretti, P., Marquet, P., Depeursinge, C., 2013. Nat. Photonics 7, 113–117.
De Bruijn, H.E., Kooyman, R.P., Greve, J., 1993. Appl. Opt. 32, 2426–2430.
De Hollander, R.B.G., Van Hulst, N.F., Kooyman, R.P.H., 1995. Ultramicroscopy 57, 263–269.
Flätgen, G., Krischer, K., Pettinger, B., Doblhofer, K., Junkes, H., Ertl, G., 1995. Science 269, 668–671.
Giebel, K.F., Bechinger, C., Herminghaus, S., Riedel, M., Leiderer, P., Weiland, U., Bastmeyer, M., 1999. Biophys. J. 76, 509–516.
Guo, K., Dong, S., Zheng, G., 2015. IEEE J. Sel. Top. Quantum Electron. 22, 77–88.
Gustafsson, M.G., 2000. J. Microsc. 198, 82–87.
Hickel, W., Kamp, D., Knoll, W., 1989. Nature 339, 186.
Jamil, M.M.A., Denyer, M.C., Youseffi, M., Britland, S.T., Liu, S., See, C.W., Somekh, M. G., Zhang, J., 2008. J. Struct. Biol. 164, 75–80.
Jenkins, A.T.A., Neumann, T., Offenhäusser, A., 2001. Langmuir 17, 265–267.
Kim, D.J., Kim, D., 2010. J. Opt. Soc. Am. B 27, 1252–1259.
Kim, K., Oh, Y., Lee, W., Kim, D., 2010. Opt. Lett. 35, 3501–3503.
Knobloch, H., von Szada-Borryszkowski, G., Woigk, S., Helms, A., Brehmer, L., 1996. Appl. Phys. Lett. 69, 2336–2337.
Kooyman, R.P.H., Krull, U.J., 1991. Langmuir 7, 1506–1509.
Kotsev, S., Dushkin, C., Ilev, I., Nagayama, K., 2003. Colloid Polym. Sci. 281, 343–352.
Kuai, Y., Chen, J., Tang, X., Xiang, Y., Lu, F., Kuang, C., Xu, L., Shen, W., Cheng, J., Gui, H., Zou, G., 2019. Sci. Adv. 5 eaav5335.
Lamprecht, B., Krenn, J.R., Schider, G., Ditlbacher, H., Salerno, M., Félidj, N., Leitner, A., Aussenegg, F.R., Weeber, J.C., 2001. Appl. Phys. Lett. 79, 51–53.
Laplatine, L., Leroy, L., Calemczuk, R., Baganizi, D., Marche, P.N., Roupioz, Y., Livache, T., 2014. Opt. Express 22, 22771–22785.
Meyer, S.A., Auguié, B., Le Ru, E.C., Etchegoin, P.G., 2012. J. Phys. Chem. A 116, 1000–1007.
Moh, K.J., Yuan, X.C., Bu, J., Zhu, S.W., Gao, B.Z., 2008. Opt. Express 16, 20734–20741.
Ou, X., Horstmeyer, R., Zheng, G., Yang, C., 2015. Opt. Express 23, 3472–3491.
Peterson, A.W., Halter, M., Tona, A., Bhadriraju, K., Plant, A.L., 2009. BMC Cell Biol. 10, 16.
Peterson, A.W., Halter, M., Tona, A., Plant, A.L., 2014. BMC Cell Biol. 15, 35.
Piscevic, D., Knoll, W., Tarlov, M.J., 1995. Supramol. Sci. 2, 99–106.
Rothenhäusler, B., Knoll, W., 1988. Nature 332, 615–617.
Schwarz, C.J., Kuznetsova, Y., Brueck, S.R.J., 2003. Opt. Lett. 28, 1424–1426.
Shan, X., Patel, U., Wang, S., Iglesias, R., Tao, N., 2010. Science 327, 1363–1366.
Shinohara, H., Sakai, Y., Mir, T.A., 2013. Anal. Biochem. 441, 185–189.
Smolyaninov, I.I., Elliott, J., Wurtz, G., Zayats, A.V., Davis, C.C., 2006. Appl. Phys. B 84, 253–256.
Somekh, M.G., Liu, S., Velinov, T.S., See, C.W., 2000. Appl. Opt. 39, 6279–6287.
Son, T., Lee, C., Seo, J., Choi, I.-H., Kim, D., 2018. Opt. Lett. 43, 959–962.
Son, T., Moon, G., Lee, H., Kim, D., 2018. Adv. Opt. Mater. 6, 1701219.
Son, T., Seo, J., Choi, I.-H., Kim, D., 2018. Opt. Commun. 422, 64–68.
Soon, C.F., Khaghani, S.A., Youseffi, M., Nayan, N., Saim, H., Britland, S., Blagden, N., Denyer, M.C.T., 2013. Colloids Surf., B 110, 156–162.
Su, Y.D., Chiu, K.C., Chang, N.S., Wu, H.L., Chen, S.J., 2010. Opt. Express 18, 20125–20135.
Thariani, R., Yager, P., 2008. Sens. Actuators, B 130, 765–770.
Toma, K., Kano, H., Offenhäusser, A., 2014. ACS Nano 8, 12612–12619.
Vander, R., Lipson, S.G., 2009. Opt. Lett. 34, 37–39.
Wang, W., Wang, S., Liu, Q., Wu, J., Tao, N., 2012. Langmuir 28, 13373–13379.
Wang, W., Yang, Y., Wang, S., Nagaraj, V.J., Liu, Q., Wu, J., Tao, N., 2012. Nat. Chem. 4, 846–853.
Watanabe, K., Matsuura, K., Kawata, F., Nagata, K., Ning, J., Kano, H., 2012. Biomed. Opt. Express 3, 354–359.
Watanabe, K., Miyazaki, R., Terakado, G., Okazaki, T., Morigaki, K., Kano, H., 2012. Biomed. Opt. Express 3, 2012–2020.
Yanase, Y., Hiragun, T., Kaneko, S., Gould, H.J., Greaves, M.W., Hide, M., 2010. Biosens. Bioelectron. 26, 674–681.
Yang, Y., Yu, H., Shan, X., Wang, W., Liu, X., Wang, S., Tao, N., 2015. Small 11, 2878–2884.
Yuk, J.S., Jung, J.W., Kim, Y.M., Ha, K.S., 2008. Sens. Actuators, B 129, 113–119.
Zhang, T., Morgan, H., Curtis, A.S.G., Riehle, M., 2001. J. Opt. A Pure Appl. Opt. 3, 333–337.
Zheng, G., Horstmeyer, R., Yang, C., 2013. Nat. Photonics 7, 739–745.